

# Hybrid Faraday rotation spectrometer for sub-ppm detection of atmospheric O<sub>2</sub>

Eric J. Zhang, Brian Brumfield, and Gerard Wysocki\*

Department of Electrical Engineering, Princeton University, Princeton, N.J. 08544, USA  
gwyssocki@princeton.edu

**Abstract:** Faraday rotation spectroscopy (FRS) of O<sub>2</sub> is performed at atmospheric conditions using a DFB diode laser and permanent rare-earth magnets. Polarization rotation is detected with a *hybrid*-FRS detection method that combines the advantages of two conventional approaches: balanced optical-detection and conventional FRS with an optimized analyzer offset angle for maximum sensitivity enhancement. A measurement precision of 0.6 ppmv·Hz<sup>-1/2</sup> for atmospheric O<sub>2</sub> has been achieved. The theoretical model of hybrid detection is described, and the calculated detection limits are in excellent agreement with experimental values.

©2012 Optical Society of America

**OCIS codes:** (300.6260) Spectroscopy, diode lasers; (300.6390) Spectroscopy, molecular; (280.4788) Optical sensing and sensors.

---

## References and links

1. R. F. Keeling, R. P. Najjar, M. L. Bender, and P. P. Tans, "What atmospheric oxygen measurements can tell us about the global carbon cycle," *Global Geochem. Cycles* **7**(1), 37–67 (1993).
2. R. F. Keeling, "Measuring correlations between atmospheric oxygen and carbon dioxide mole fractions: a preliminary study in urban air," *J. Atmos. Chem.* **7**(2), 153–176 (1988).
3. R. Kocache, "The measurement of oxygen in gas mixtures," *J. Phys. E Sci. Instrum.* **19**(6), 401–412 (1986).
4. O. S. Wolfbeis and M. J. P. Leiner, "Recent progress in optical oxygen sensing," *Proc. SPIE* **906**, 42–48 (1988).
5. A. A. Gorman and M. A. J. Rodgers, "Current perspectives of singlet oxygen detection in biological environments," *J. Photochem. Photobiol. B* **14**(3), 159–176 (1992).
6. D. B. Papkovsky, "Methods in optical oxygen sensing: protocols and critical analyses," *Methods Enzymol.* **381**, 715–735 (2004).
7. L. Pauling, R. E. Wood, and J. H. Sturdivant, "An instrument for determining the partial pressure of oxygen in a gas," *J. Am. Chem. Soc.* **68**(5), 795–798 (1946).
8. R. P. Kovacich, N. A. Martin, M. G. Clift, C. Stocks, I. Gaskin, and J. Hobby, "Highly accurate measurement of oxygen using a paramagnetic gas sensor," *Meas. Sci. Technol.* **17**(6), 1579–1585 (2006).
9. M. Benammar, "Techniques for measurement of oxygen and air-to-fuel ratio using zirconia sensors. A review," *Meas. Sci. Technol.* **5**(7), 757–767 (1994).
10. J. Ye, Y. Wen, W. D. Zhang, H. Cui, L. M. Gan, G. Q. Xu, and F. Sheu, "Application of multi-walled carbon nanotubes functionalized with hemin for oxygen detection in neutral solution," *J. Electroanal. Chem.* **562**(2), 241–246 (2004).
11. Z. Fan, D. Wang, P. Chang, W. Tseng, and J. G. Liu, "ZnO nanowire field-effect transistor and oxygen sensing property," *Appl. Phys. Lett.* **85**(24), 5923–5925 (2004).
12. P. Vogel and V. Ebert, "Near shot noise detection of oxygen in the A-band with vertical-cavity surface-emitting lasers," *Appl. Phys. B* **72**(1), 127–135 (2001).
13. V. Weldon, J. O'Gorman, J. J. Perez-Camacho, D. McDonald, J. Hegarty, J. C. Connolly, N. A. Morris, R. U. Martinelli, and J. H. Abeles, "Laser diode based oxygen sensing: A comparison of VCSEL and DFB laser diodes emitting in the 762 nm region," *Infrared Phys. Technol.* **38**(6), 325–329 (1997).
14. Q. V. Nguyen, R. W. Dibble, and T. Day, "High-resolution oxygen absorption spectrum obtained with an external-cavity continuously tunable diode laser," *Opt. Lett.* **19**(24), 2134–2136 (1994).
15. D. M. Bruce and D. T. Cassidy, "Detection of oxygen using short external cavity GaAs semiconductor diode lasers," *Appl. Opt.* **29**(9), 1327–1332 (1990).
16. C. Corsi, M. Gabrysch, and M. Inguscio, "Detection of molecular oxygen at high temperature using a DFB-diode-laser at 761 nm," *Opt. Commun.* **128**(1-3), 35–40 (1996).
17. M. Kroll, J. A. McClintock, and O. Ollinger, "Measurement of gaseous oxygen using diode laser spectroscopy," *Appl. Phys. Lett.* **51**(18), 1465–1467 (1987).
18. A. Pohlkötter, M. Köhring, U. Willer, and W. Schade, "Detection of molecular oxygen at low concentrations using quartz enhanced photoacoustic spectroscopy," *Sensors (Basel)* **10**(9), 8466–8477 (2010).

19. R. J. Brecha, L. M. Pedrotti, and D. Krause, "Magnetic rotation spectroscopy of molecular oxygen with a diode laser," *J. Opt. Soc. Am. B* **14**(8), 1921–1930 (1997).
20. L. Gianfrani, R. W. Fox, and L. Hollberg, "Cavity-enhanced absorption spectroscopy of molecular oxygen," *J. Opt. Soc. Am. B* **16**(12), 2247–2254 (1999).
21. P. A. S. Jorge, P. Caldas, C. C. Rosa, A. G. Oliva, and J. L. Santos, "Optical fiber probes for fluorescence based oxygen sensing," *Sens. Actuators* **103**(1-2), 290–299 (2004).
22. B. G. Stephens, R. F. Keeling, and W. J. Paplawsky, "Shipboard measurements of atmospheric oxygen using a vacuum-ultraviolet absorption technique," *Tellus B Chem. Phys. Meteorol.* **55**(4), 857–878 (2003).
23. M. K. Krihak and M. R. Shahriari, "Highly sensitive, all solid state fiber optic oxygen sensor based on the sol-gel coating technique," *Electron. Lett.* **32**(3), 240–242 (1996).
24. B. Brumfield and G. Wysocki, "Faraday rotation spectroscopy based on permanent magnets for sensitive detection of oxygen at atmospheric conditions," *Opt. Express* **20**(28), 29727–29742 (2012).
25. S. G. So, E. Jeng, and G. Wysocki, "VCSEL based Faraday rotation spectroscopy with a modulated and static magnetic field for trace molecular oxygen detection," *Appl. Phys. B* **102**(2), 279–291 (2011).
26. S. G. So, O. Marchat, E. Jeng, and G. Wysocki, "Ultra-sensitive Faraday rotation spectroscopy of O<sub>2</sub>: model vs. experiment," CLEO (Baltimore, Maryland 2011), CThT2.
27. L. R. Brown and C. Plymate, "Experimental line parameters of the oxygen A band at 760 nm," *J. Mol. Spectrosc.* **199**(2), 166–179 (2000).
28. R. Lewicki, J. H. Doty 3rd, R. F. Curl, F. K. Tittel, and G. Wysocki, "Ultrasensitive detection of nitric oxide at 5.33 microm by using external cavity quantum cascade laser-based Faraday rotation spectroscopy," *Proc. Natl. Acad. Sci. U.S.A.* **106**(31), 12587–12592 (2009).
29. V. S. Zapasskii, "Highly sensitive polarimetric techniques," *J. Appl. Spectrosc.* **37**(2), 181–196 (1982).
30. H. Adams, D. Reinert, P. Kalkert, and W. Urban, "A differential detection scheme for Faraday rotation spectroscopy with a color center laser," *Appl. Phys. B* **34**(4), 179–185 (1984).
31. R. F. Curl, F. Capasso, C. Gmachl, A. Kosterev, B. McManus, R. Lewicki, M. Pusharsky, G. Wysocki, and F. K. Tittel, "Quantum cascade lasers in chemical physics," *Chem. Phys. Lett.* **487**(1-3), 1–18 (2010).
32. J. Hodgkinson and R. P. Tatam, "Optical gas sensing: a review," *Meas. Sci. Technol.* **24**(1), 012004 (2013).
33. M. Nikodem and G. Wysocki, "Measuring optically thick molecular samples using chirped laser dispersion spectroscopy," *Opt. Lett.* **38**(19), 3834–3837 (2013).

## 1. Introduction

The significant role of oxygen in geochemical and biological cycles necessitates its detection in various scientific and environmental settings [1–6]. Modern applications are increasingly stringent, requiring greater accuracy, stability and shorter acquisition times [1, 3]. Magnetodynamic detection of oxygen by exploiting its paramagnetic properties is one technique that has been explored to meet these requirements [7, 8], but is susceptible to mechanical vibrations and drifts. Alternate techniques include solid-state sensors for combustion diagnostics [9], and more recently miniature oxygen sensors, where alteration of the electrical or chemical properties of nanostructures is used [10, 11]. Despite substantial progress in oxygen detection technologies, *in situ* oxygen detection remains challenging due to issues involving environmental contamination, operating pressure constraints and interfering molecular species.

Optical spectroscopic systems have received strong interest due to their sensitivity and specificity [12–21] and are frequently built for low-power, field deployable operation. Sub-part-per-million (sub-ppmv) oxygen detection limits have been achieved with vacuum-ultraviolet absorption [22] and fiber-based techniques [23], although portability, dynamic range and *in situ* capabilities hinder their application. To date, we have not identified any sensor in literature that performs *in situ* atmospheric oxygen detection with the target sub-ppmv sensitivity required for biorespiratory diagnostics.

Recent work [24–26] has identified promise for sub-ppmv oxygen detection at atmospheric pressure using Faraday rotation spectroscopy (FRS) that targets the A-band of oxygen at 762 nm. In FRS, an applied magnetic field splits the  $^3\Sigma_g$  oxygen ground state, and quantum selection rules allow only  $\Delta M_j = +1$  and  $-1$  for rovibronic transitions in the A-band, which interact with right-handed and left-handed circularly polarized light respectively. This creates circular birefringence, which causes rotation of linearly polarized light as it travels through an oxygen sample, and is detected by projection onto a nearly-crossed polarizer. So et al. [25, 26] performed atmospheric pressure FRS on the oxygen  $^1P_1(1)$  transition in the A-band [27] using a modulated (AC) magnetic field, yielding an AC-FRS detection limit of  $10 \text{ ppmv}\cdot\text{Hz}^{-1/2}$ . Brumfield et al. [24] employed rare-earth magnets for static

(DC) field generation and conventional balanced-detection FRS for fringe removal and intensity-noise suppression. This configuration was used to achieve a shot-noise limited sensitivity of  $6 \text{ ppmv} \cdot \text{Hz}^{-1/2}$ .

In the present work we demonstrate further sensitivity enhancement using a distributed-feedback (DFB) laser diode and a *hybrid*-FRS system that combines balanced optical detection and optimization of the analyzer offset angle typical for conventional AC-FRS systems. The hybrid-FRS technique, which also uses a DC magnetic field, achieves a  $10\times$  enhancement beyond the sensitivity reported in [24].

## 2. Conventional FRS methods

There are two distinct FRS signal detection methods reported in literature: **(1)**  $90^\circ$ -method implemented with nearly-crossed polarizers [26, 28, 29] and **(2)**  $45^\circ$ -method employing balanced optical detection [29–31]. The  $90^\circ$ -method is more popular [28, 31] because it is simpler to implement, requiring only a single photodetector and two nearly-crossed polarizers (one before and after the gas sample) to measure the Faraday rotation of the light polarization [31]. In this nearly-crossed polarizer configuration, the laser noise is effectively suppressed, providing an improved signal-to-noise (SNR) ratio in the FRS measurement compared to direct absorption spectroscopy. The optimum analyzer uncrossing angle ( $\alpha_{opt}$ ) is determined by equalizing the detector-noise equivalent power (NEP) with the laser intensity noise or quantum shot noise generated from the laser radiation incident on the photodetector. In the  $45^\circ$ -method, the laser noise suppression is performed electronically by splitting the laser beam emerging from the sample cell into two orthogonally polarized components (usually of equal power achieved with  $\alpha = 45^\circ$ ) and performing balanced optical detection using two photodetector elements. In this configuration, the component FRS signals measured on both photodetector elements are out of phase, while the intensity-noise is in phase allowing for effective laser-noise suppression. Auto-balancing photodetectors (e.g. Nirvana auto-balancing photodetector by New Focus) that require other than a 50/50 split ratio have also been successfully used in balanced detection FRS systems (the split ratio can be conveniently adjusted by varying  $\alpha$ ) [24]. Prior experimental work has assumed the  $45^\circ$ -method and the  $90^\circ$ -method to be separate [28, 30, 31]; that is, the use of one method precludes the other. In what follows, we experimentally show that these two techniques can be used in a complementary fashion resulting in a hybrid-FRS method that can achieve a better SNR than either one alone. To identify the benefits of hybrid-FRS, we compare below the performance of hybrid-FRS with the conventional  $45^\circ$ -method and  $90^\circ$ -method.

## 3. Experimental setup

The studies and experiments have been performed using the optical configuration shown in Fig. 1. The setup is similar to that reported by Brumfield et al. [24], but the VCSEL laser used in [24] has been replaced with a DFB diode laser (Sacher Lasertechnik,  $\lambda = 762 \text{ nm}$ ), with small modifications made to the polarization optics to enable hybrid-FRS measurement. The DFB laser targets the  ${}^{\text{P}}\text{P}_1(1)$   $\text{O}_2$  transition in the A electronic band. The laser current is modulated at 6 kHz with a modulation depth optimized to maximize the second-harmonic ( $2f$ )

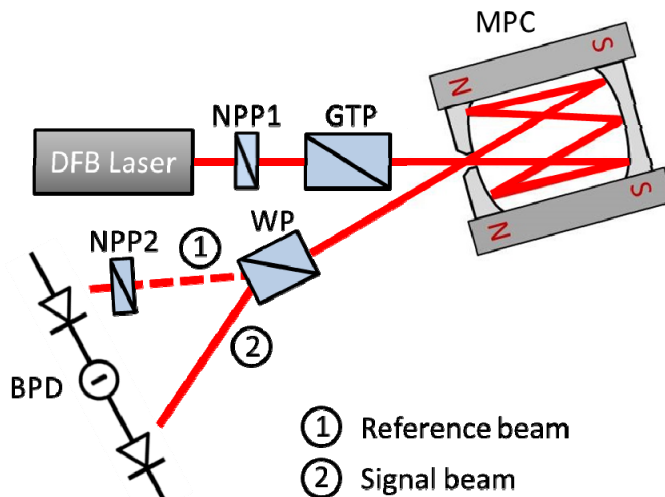


Fig. 1. Optical layout of the FRS setup used in this study. The DFB laser output power is attenuated using a NPP (NPP1), and polarized by the GTP prior to entering the MPC. The signal beam exiting the MPC passes through a WP and is detected by the BPD. The NPP2 attenuates the reference beam to prevent optical saturation of the reference-photodiode. **Abbreviations:** DFB: distributed-feedback; GTP: Glan-Thompson polarizer; MPC: multi-pass cell; WP: Wollaston prism; NPP: nano-particle polarizer; BPD: balanced-photodetector.

FRS signal. The ambient laboratory air at room temperature and atmospheric pressure is used as the sample gas for our studies. The laser light is first transmitted through a Glan-Thompson polarizer (GTP) to establish a clean polarization state prior to entering a cylindrical-mirror multi-pass cell (MPC). The cell provides 6.8 m path length with 40% optical throughput. An array of rare-earth magnets generates a 554 Gauss axial magnetic field in the active region probed by the laser beam within the multi-pass cell. Light passing through the cell undergoes polarization rotation due to interaction with the sample and is split (after exiting the cell) into orthogonal components by a Wollaston prism (WP). Balanced detection and demodulation is performed using a Nirvana auto-balancing photodetector (New Focus, model 2007) and lock-in amplifier (Signal Recovery 7265), with automated data acquisition using a DAQ board (NI-USB-6529) and customized LabVIEW software. The auto-balancing function is employed with an optimal 2:1 reference- to signal-photodiode split-ratio (480  $\mu$ W on the signal-photodiode), resulting in laser intensity-noise suppression of  $> 20$  dB (the 21.6 dB common-mode rejection ratio (CMRR) of the balanced detector was determined experimentally). The system is used to perform detection using the  $45^\circ$ -method and hybrid-FRS methods. As the DFB laser is capable of providing up to 30 mW of output optical power, a nano-particle polarizer (NPP) (shown as NPP1 in Fig. 1) is placed just at the laser output to attenuate the laser radiation and avoid detector saturation in the  $45^\circ$ -method. In hybrid-FRS the NPP1 is set to maximum transmission and the detector saturation is avoided by combination of the appropriate  $\alpha$  setting and attenuation of the reference branch using the NPP2 (see Fig. 1). Since the optical fringes introduced by the NPP2 are very stable, the auto-balancing circuit is capable of compensation of any slow optical power drift between the reference- and signal-photodiodes. It should also be noted that NPP2 is relatively thin resulting in a large fringe free spectral range ( $> 10\times$  the  $P_{1(1)}$  linewidth), so any parasitic intensity modulation induced by the laser wavelength modulation creates a negligible baseline offset in the measured FRS signal.

In order to assess the proposed hybrid FRS method and establish a performance baseline, conventional balanced detection FRS has been implemented using the same system components. In our prior work we used a VCSEL [24] capable of delivering 20  $\mu$ W of optical power to the signal-photodiode. This resulted in a minimum detection limit (MDL) for  $O_2$  of

6 ppmv·Hz<sup>-1/2</sup>. Application of a more powerful DFB laser that can easily deliver up to 480 μW to the signal-photodetector (detector saturation occurs at 500 μW) is expected to result in a 4.9× improvement in sensitivity to oxygen. At  $P_0 \approx 1.4$  mW (which provides 480 μW to the signal detector at split ratio of 2:1), the MDL for O<sub>2</sub> measured with the conventional balanced FRS system using DFB laser is 1.8 ppmv·Hz<sup>-1/2</sup>. This corresponds to an improvement of 3.3×, or 70% of the expected enhancement. The 30% discrepancy has been attributed to the higher laser relative intensity-noise (RIN) of  $5.3 \times 10^{-7}$  Hz<sup>-1/2</sup> (2× the VCSEL RIN), and an order of magnitude smaller CMRR. At these conditions the 45°-method operates roughly at 2× the quantum shot-noise limit. However, it should be noted that due to the detector saturation limit only a fraction of the available laser power ( $P_0 \approx 1.4$  mW vs. 8 mW maximum available after the MPC) could be used to perform this measurement.

### 3.1 Limitations of the 45°- and 90°-method

Based on the results obtained with the 45°-method in the previous section, one can realize that its main limitation is related to detector saturation, which limits the amount of total laser power that can be used in the FRS measurement. On the contrary, the 90°-method is free from this limitation, because the amount of light transmitted through a nearly crossed analyzer is significantly lower; however, laser-noise and electromagnetic interference limit its sensitivity. In order to discuss the main limitations in both techniques, an analysis of signal and noise in both methods is performed below.

In the 45°-method, the signal ( $V_{45^\circ}$ ) and noise ( $\sigma_{45^\circ}$ ) can be expressed as:

$$V_{45^\circ} = 2 \cdot G \cdot R_i \cdot P_0 \cdot \Theta \quad (1)$$

$$\sigma_{45^\circ} = \sqrt{[G \cdot R_i \cdot NEP]^2 + [G \cdot \sqrt{4q \cdot R_i \cdot \frac{P_0}{2}}]^2 + [10^{-\frac{CMRR}{20}} \cdot G \cdot R_i \cdot RIN \cdot \frac{P_0}{2}]^2} \quad (2)$$

Where  $G = 10^5$  V/A is the transimpedance gain,  $R_i = 0.5$  A/W is the detector responsivity, and  $P_0$  and  $\Theta$  are the incident power (Watts) on the analyzer and polarization rotation angle in radians (due to the Faraday Effect) respectively. Similarly, in the 90°-method the signal and noise can be expressed as:

$$V_{90^\circ} = G \cdot R_i \cdot P_0 \cdot [\sin(2\alpha)] \cdot \Theta \quad (3)$$

$$\sigma_{90^\circ} = \sqrt{[G \cdot R_i \cdot NEP]^2 + [G \cdot \sqrt{2q \cdot R_i \cdot P_0 \sin^2 \alpha}]^2 + [G \cdot R_i \cdot RIN \cdot P_0 \sin^2 \alpha]^2} \quad (4)$$

Theoretically both techniques can ultimately be shot-noise limited. With an assumption that the shot-noise limit is achieved when the photocurrent shot-noise becomes equal to either the detector- or laser-noise, one can express the total noise of the system as:

$$\sigma_{45^\circ-SN} = \sqrt{2}G \cdot \sqrt{4q \cdot R_i \cdot \frac{P_0}{2}} = G \cdot \sqrt{4q \cdot R_i \cdot P_0} \quad (5)$$

$$\sigma_{90^\circ-SN} = \sqrt{2}G \cdot \sqrt{2q \cdot R_i \cdot P_0 \sin^2 \alpha} = G \cdot \sqrt{4q \cdot R_i \cdot P_0 \sin^2 \alpha} \quad (6)$$

The factor  $\sqrt{2}$  represents a quadrature sum of two noise contributions of the same magnitude. The SNR in the shot-noise limited ( $SNR_{SN}$ ) case for both methods becomes:

$$SNR_{45^\circ-SN} = \frac{V_{45^\circ}}{\sigma_{45^\circ-SN}} = \sqrt{\frac{R_i \cdot P_0}{q}} \Theta \quad (7)$$

$$SNR_{90^\circ-SN} = \frac{V_{90^\circ}}{\sigma_{90^\circ-SN}} = \sqrt{\frac{R_i \cdot P_0}{q}} \cos(\alpha) \Theta \quad (8)$$

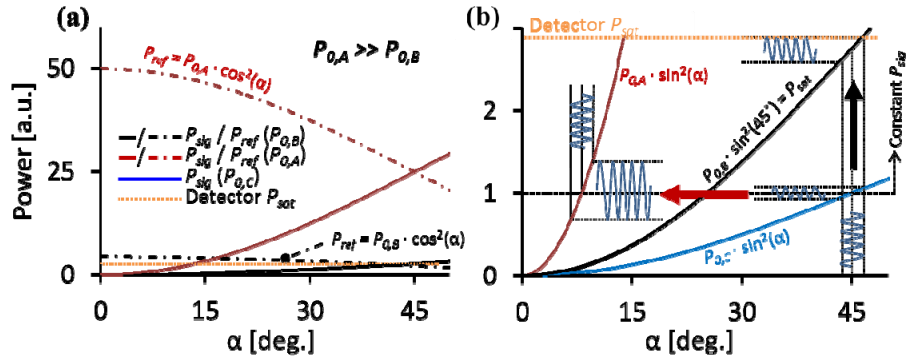


Fig. 2. (a) Malus' law for the signal- and reference-photodiodes, with a high-power (red curve, hybrid-FRS) and low-power (black curve, 45°-method) case. The low-power case ( $P_{0,B}$ ) can be used for conventional balanced detection when both signal and reference branches are below detector saturation. (b) In conventional balanced detection using low-power, signal enhancement (black arrow) is achieved by increasing  $P_{0,C}$  to  $P_{0,B}$  (detector saturation, or intensity- and shot-noise crossover point). In hybrid-FRS,  $P_{0,C}$  increases to  $P_{0,A}$  (red arrow) with decreasing  $\alpha$  at constant  $P_{sig}$  (thus constant noise). Signal  $\sim 1/\alpha$  for small  $\alpha$ , hence SNR  $\sim 1/\alpha \sim P_0^{1/2}$ . Hybrid-FRS avoids saturation and intensity-noise limitations by moving the operating point parallel rather than perpendicular to the  $\alpha$ -axis.

Therefore with an assumption of  $\alpha < 10^\circ$  in the 90°-method both techniques should provide comparable ultimate performance. However practical limitations exist, and result in SNRs significantly lower than  $SNR_{SN}$  in both techniques.

#### (A) Detector saturation limit in 45°-method

Given the total laser power on each detector element is limited by the specified saturation power  $P_{sat}$ , there is a limit to the total power  $P_0$  that can be used in the FRS measurement. To understand this point, we may consider a high power ( $P_{0,A}$ ) and low power ( $P_{0,B}$ ) case of Malus' law in Fig. 2(a), where conventional balanced detection may be used in the case of  $P_{0,B}$  (since both signal and reference branches are below saturation, Fig. 2(b)). Using small signal analysis and assuming shot-noise domination (Eq. (7)), it is clear that SNR enhancement will require increasing  $P_{0,B}$ , and is limited by detector saturation, i.e.  $P_{0,B} < P_{sat}$ . Thus despite excellent laser-noise suppression provided by the balanced detection that enables operation in the shot-noise regime, there is a hard limit in the maximum achievable SNR with this technique. Therefore application of more powerful lasers does not bring the  $P_0^{1/2}$  improvement in SNR predicted by Eq. (7), but only allows for maximum power of  $P_0 = 2P_{sat}$  which limits the ultimate performance of the system.

#### (B) Laser noise limit in 90°-method

As predicted by Eq. (8), the 90°-method should be capable of the same ultimate sensitivity as provided by the shot-noise limited 45°-method. However the lack of balanced detection that provides an additional 20 dB of CMRR makes it difficult to suppress the laser-noise in the FRS system using the 90°-method. As a result, the laser-noise suppression based solely on the optical suppression through a decrease in  $\alpha$  may not be sufficient to achieve shot-noise limited operation (please note that the signal in Eq. (3) scales with  $\sin(2\alpha)$  while the laser-noise is proportional to  $\sin^2(\alpha)$ , which allows for improvement in SNR in the laser-noise dominated regime by decreasing  $\alpha$  until the detector-noise floor is reached; in such a configuration the shot-noise limited operation can only be obtained with ultra-low noise photodetectors and high-quality polarizers). Therefore most of the FRS systems utilizing the

90°-method operate in the laser intensity-noise dominated regime. Using Eqs. (3) and (4) and the experimental parameters relevant to our setup with  $NEP = 5.4 \times 10^{-12} \text{ pW} \cdot \text{Hz}^{-1/2}$ ,  $RIN = 5.3 \times 10^{-7} \text{ Hz}^{-1/2}$ , and  $P_0 = 8 \text{ mW}$  (obtained from our 30 mW DFB diode after optical losses in the system primarily

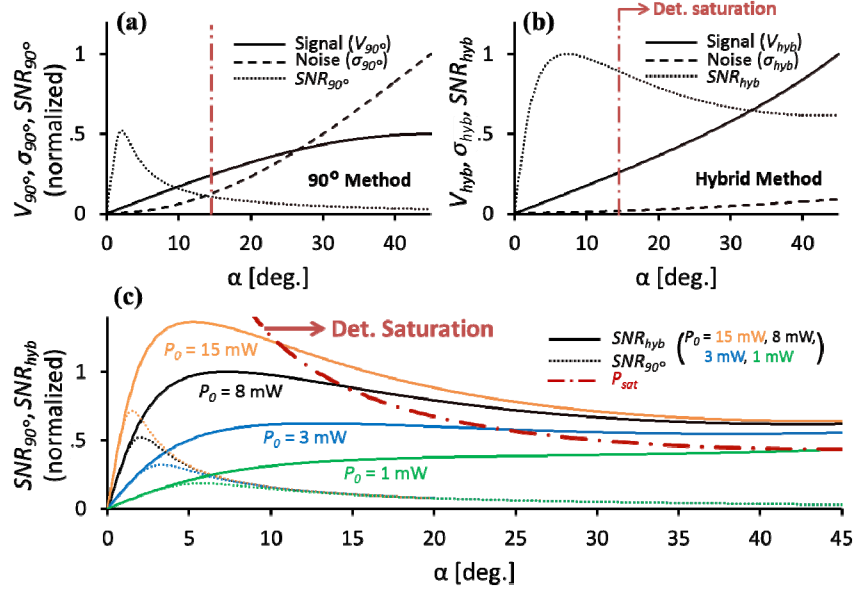


Fig. 3. Hybrid-FRS and 90°-method SNR calculation. (a) SNR for 90°-method at  $P_0 = 8 \text{ mW}$ . For small  $\alpha$ , noise  $\sim \alpha^2$  and signal  $\sim \alpha$ . (b) SNR for hybrid-FRS at the same  $P_0$ . CMRR suppression of intensity-noise gives significant SNR increase.  $V_{90^\circ}$  is normalized to the  $V_{hyb}$  maximum,  $\sigma_{hyb}$  is normalized to the  $\sigma_{90^\circ}$  maximum, and  $SNR_{90^\circ}$  is normalized to maximum of  $SNR_{hyb}$ . (c) Multiple SNR plots for  $P_0 = 1 \text{ mW}$ ,  $3 \text{ mW}$ ,  $8 \text{ mW}$  and  $15 \text{ mW}$ . From the curves it is clear that  $SNR_{hybrid} \geq SNR_{90^\circ}$ . The shaded red regions indicate the disallowed operating regime due to the limitation of detector saturation.

from the MPC), the best  $SNR_{90^\circ}$  is achieved at  $2^\circ$  as shown in Fig. 3(a). For ease of comparison, the  $SNR_{90^\circ}$  values presented in Fig. 3(b) were normalized to the peak SNR of the hybrid-FRS method at  $P_0 = 8 \text{ mW}$ .

#### 4. Hybrid-FRS

Theoretically, the benefit of hybrid-FRS can be explained using SNR calculations. The hybrid-FRS signal equation is derived as balanced detection for an arbitrary  $\alpha$  ( $0 < \alpha < 45^\circ$ ), with the NPP2 polarizer (Fig. 1) and auto-balancing circuit suppressing  $P_{ref}$  by  $\gamma = \tan^2(\alpha)$  and analyzing the difference  $P_{sig} - \gamma P_{ref}$ , which yields [24]:

$$V_{hybrid} = G \cdot R_i \cdot P_0 \cdot [(1 + \gamma) \cdot \sin(2\alpha)] \cdot \Theta \quad (9)$$

We may also consider the noise of the hybrid-FRS, given as the quadrature sum of detector-, shot- and laser intensity-noise:

$$\sigma_{hybrid} = \sqrt{[G \cdot R_i \cdot NEP]^2 + [G \cdot \sqrt{4q \cdot R_i \cdot P_0 \sin^2 \alpha}]^2 + [10^{\frac{CMRR}{20}} \cdot G \cdot R_i \cdot RIN \cdot P_0 \sin^2 \alpha]^2} \quad (10)$$

When shot-noise limited operation is achieved the total noise of the system can be expressed as:

$$\sigma_{\text{hybrid-SN}} = \sqrt{2}G \cdot \sqrt{4q \cdot R_i \cdot P_0 \sin^2 \alpha} \quad (11)$$

and the SNR in the shot-noise limited case becomes:

$$\text{SNR}_{\text{hybrid-SN}} = \frac{V_{\text{hybrid}}}{\sigma_{\text{hybrid-SN}}} = \frac{\sin(\alpha) + \cos(\alpha)}{\sqrt{2}} \sqrt{\frac{R_i \cdot P_0}{q}} \Theta \quad (12)$$

It is clear that in the case of  $\alpha = 45^\circ$  the shot-noise limited SNR for the hybrid method becomes equivalent to Eq. (7) derived for 45°-method. For small  $\alpha$ , the ultimate shot-noise limited SNR tends to be slightly smaller ( $\sqrt{2}$  times) than  $\text{SNR}_{90^\circ\text{-SN}}$  in Eq. (8). However given the effective laser noise suppression through balanced detection that helps in approaching the shot-noise limited regime, a  $\sqrt{2}$  decrease in the ultimate SNR represents only a small penalty for the use of a second detector (the  $\sqrt{2}$  factor originates from the second detector contributing uncorrelated photocurrent shot-noise).

#### 4.1 Comparison of hybrid-FRS to 45°- and 90°-methods

The impact of laser noise suppression through balanced detection in hybrid-FRS is clearly noticeable in Figs. 3(a) and 3(b) which compare the  $\text{SNR}_{\text{hybrid}}$  with SNR achievable with the conventional 90°-method using experimental parameters relevant to our optical setup. For easier comparison all values of the SNR presented in the Fig. 3 are normalized to the maximum SNR achieved with the hybrid method at  $P_0 = 8$  mW. For the maximum  $P_0$  of 8 mW, the 90°-method achieves optimum operating conditions at  $\alpha_{\text{opt.}} = 2^\circ$  with the SNR nearly  $\frac{1}{2}$  of that achievable with hybrid-FRS. The hybrid method achieves an optimal SNR at  $\alpha_{\text{opt.}} = 7.3^\circ$ , indicating a lower effective laser noise achieved with the balanced detection that permits opening the analyzer further to increase the laser power on the photodetector. Similar calculations were performed for other laser powers with an assumption of the same RIN and NEP. Figure 3(c) shows that in all cases the hybrid method demonstrates better performance than the 90°-method. It is also clear that for low-power lasers (e.g. VCSELs, see the  $P_0 = 1$  mW plot) there may be no optimum point on the SNR plot and the  $\alpha_{\text{opt.}}$  becomes  $45^\circ$ , making hybrid-FRS equivalent to the conventional 45°-method.

In the case of low laser power such that the incident power on the signal-photodiode remains always below detector saturation even at an analyzer uncrossing angle of  $\alpha = 45^\circ$  ( $P_{\text{sig}} = P_0/2$ ) (Fig. 3(c)), the 45°-method is usually expected to provide better performance than the 90°-method. This is due to efficient laser noise suppression by balanced detection while operating the FRS system at the point of maximum signal generated at  $\alpha = 45^\circ$ . This is also indicated in Fig. 3(c) that shows  $\text{SNR}_{90^\circ}$  and  $\text{SNR}_{\text{hybrid}}$  at  $P_0 = 1$  mW (effectively  $\text{SNR}_{45^\circ}$ ) as a function of  $\alpha$  for low power. If the conventional 45°-method is used the  $\text{SNR}_{45^\circ}$  can only be improved through an increase of optical power, but once the detector saturation is reached, further increase of signal in the 45°-method is not possible (see black line in Fig. 2(b)). Therefore at higher laser power it is beneficial to use hybrid-FRS and decrease  $\alpha$  to achieve an increase in FRS signal while keeping the  $P_{\text{sig}}$  constant and below detector saturation (see red line in Fig. 2(b)). If the laser noise is effectively suppressed by the balanced detector, the shot-noise limited operation can be maintained and SNR follows the  $P_0^{1/2}$  increase predicted by Eq. (12).

In conclusion hybrid-FRS eliminates the detector-saturation limitation of 45°-method and reduces intensity-noise through balanced detection, thus enabling shot-noise limited operation that is rarely achieved in practice with the conventional 90°-method.

#### 4.2 Power constraints

We now consider minimum and maximum power limitations in hybrid-FRS. It has been observed in Fig. 3(c) for the given experimental parameters, that when  $P_0$  is low ( $\sim 1$  mW), the SNR curve increases monotonically with no local maximum. In this case we see that there exists a minimum power  $P_{0,\text{min}}$  under which no benefit is derived from decreasing  $\alpha$ , and

conventional balanced detection is superior (i.e. one should work as close as possible to  $45^\circ$  when operating below saturation of the balanced-photodetector). One can solve for this condition as the minimum laser power which satisfies  $d(\text{SNR})/d\alpha = 0$  for  $0^\circ < \alpha < 45^\circ$ . The angle  $\alpha$  where  $d(\text{SNR})/d\alpha = 0$  is the optimal crossing angle  $\alpha_{\text{opt}}$ , which is plotted for varying

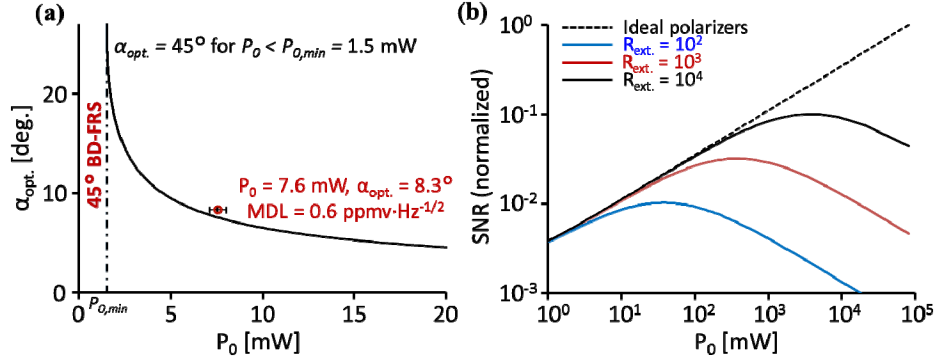


Fig. 4. (a) Minimum power constraint. Optimum crossing angle  $\alpha_{\text{opt}}$  vs.  $P_0$  on balanced-photodetector (solid black line). For  $P_0 < P_{0,\text{min}}$  no SNR local maximum exists, and conventional balanced detection is superior. The red circle is our experimental operating point. (b) Maximum power constraint. Finite polarization extinction ratio will cause light to leak through the nearly-crossed GTP and WP for large  $P_0$  and small  $\alpha$ . The leakage optical power introduces more noise than would otherwise be present. Each curve corresponds to traveling along a line of  $P_{\text{sig}} = 160 \mu\text{W}$  in Fig. 5(c), and SNR values are normalized to the maximum SNR at  $P_0$  of  $10^5$  mW calculated for the ideal polarizers.

$P_0$  in Fig. 4(a). We calculate that below  $P_{0,\text{min}} = 1.5$  mW our system requires conventional balanced detection, while for  $P_0 > 1.5$  mW hybrid-FRS becomes optimal.

To optimize system performance, the operating point should lie upon the solid black line in Fig. 4(a), while maximizing available laser power  $P_0$ . Our experimental operating point is indicated by the red circle, with  $\alpha = 8.3^\circ$  at  $P_0 = 7.6$  mW, which is close to the theoretical  $\alpha_{\text{opt}} = 7.5^\circ$ . Slight deviations of  $\alpha$  do not affect the SNR as each point on Fig. 4(a) represents a zero-derivative SNR condition.

To estimate the maximum power limit one has to consider polarization extinction ratio ( $R_{\text{ext}}$ ), which has been neglected so far but will play a significant role for large  $P_0$  and small  $\alpha$ , as light leakage will be comparable to the total power transmitted through an ideal polarizer. This effect of finite  $R_{\text{ext}}$  manifests itself as a transformation of the reference-photodiode suppression factor  $\gamma \rightarrow \gamma \cdot \zeta$  in Eq. (9), and signal power  $P_0 \cdot \sin^2(\alpha) \rightarrow P_0 \cdot \sin^2(\alpha) \cdot \zeta$  in Eq. (10) where  $\zeta = 1 + (\gamma R_{\text{ext}})^{-1}$ . The effect of the non-ideal polarizers is shown in Fig. 4(b) which shows SNR as a function of  $P_0$  for different  $R_{\text{ext}}$ . The SNR indeed increases as  $P_0^{1/2}$  but only until the laser-noise leaking through the polarizers begins to dominate and outweighs any benefit derived from increasing  $P_0$ . In our experiment, although the GTP and WP have  $R_{\text{ext}} \sim 10^4$ , due to depolarization in the MPC an effective extinction ratio of  $R_{\text{ext}} \sim 10^3$  has been determined (corresponding to the red curve in Fig. 4(b)). Therefore in our current system the maximum power limit is  $\sim 100$  mW, beyond which little or no SNR improvement is expected.

## 5. Hybrid-FRS: measurement results

Hybrid-FRS measurements were performed using the system in Fig. 1. The hybrid system is optimized subject to limitations of detector-noise (dominating at  $P_{\text{sig}} < 20 \mu\text{W}$ ), intensity-noise (dominating at  $P_{\text{sig}} > 660 \mu\text{W}$ ), detector saturation (occurring at  $P_{\text{sig}} = 500 \mu\text{W}$ ) and laser power available for measurement of  $P_0 = 8$  mW. Figure 5(a) shows a plot of total noise as a function of optical power  $P_0$  and analyzer offset angle  $\alpha$  derived from experimental measurements of laser- and detector-noise. Since each constraint is delimited by a given  $P_{\text{sig}}$ , the curves determining the operation area of the system follow the form of  $P_0 = P_{\text{sig}}/\sin^2(\alpha)$ .

The laser intensity-noise is calculated assuming a CMRR of  $21.6 \text{ dB} \pm 1.8 \text{ dB}$ , determined as an average from numerous measurements over different optical powers and split ratios.

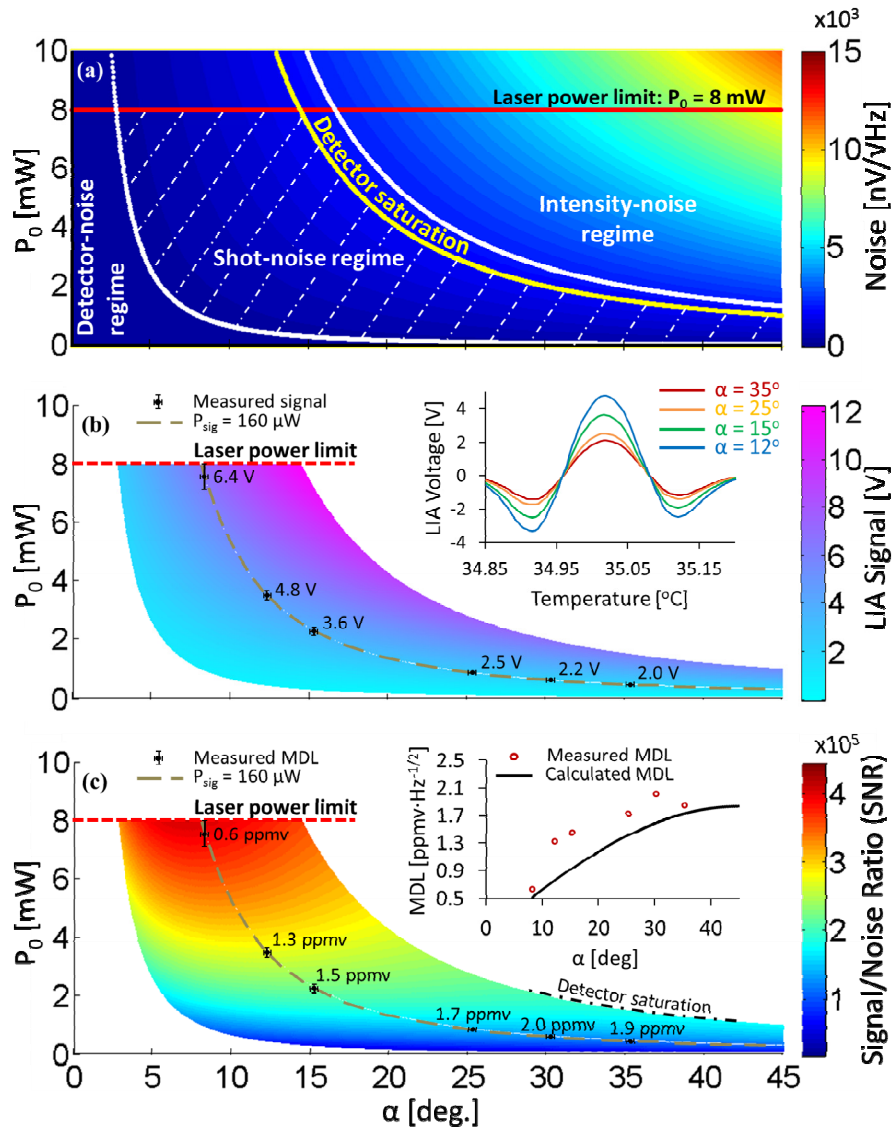


Fig. 5. (a) Operating parameter space for the hybrid-FRS method.  $\alpha$  is the crossing angle between the WP and GTP.  $P_0$  is the total power incident upon the balanced detector. The desired shot-noise region of operation is indicated by the dashed lines. Each of the curves corresponds to a line of constant  $P_{sig}$ ;  $P_{sig} < 20 \mu\text{W}$  in detector-noise regime,  $P_{sig} > 500 \mu\text{W}$  for detector saturation and  $P_{sig} > 660 \mu\text{W}$  in intensity-noise regime. The red horizontal line defines the power output limit of the DFB laser after accounting for optical losses of the system. (b) Calculated signals with measurements superimposed (black points), which lie upon a line of constant  $P_{sig} = 160 \mu\text{W}$  (dashed curve). The inset shows four measured  $2f$  DC-FRS signals at varying  $\alpha$ . (c) Calculated SNR for hybrid-FRS parameter space. Black points indicate measurements along  $P_{sig} = 160 \mu\text{W}$ . An MDL of  $0.6 \text{ ppmv} \cdot \text{Hz}^{-1/2}$  is achieved at  $\alpha = 8.3^\circ$  ( $\alpha_{opt} = 7.5^\circ$ ), which is  $1.4 \times$  the shot-noise limit. The inset shows a comparison of measured detection limits and those calculated from the SNR at  $P_{sig} = 160 \mu\text{W}$  (the size of the red circles indicate the measurement error).

It is always desirable to operate in the shot-noise regime (shaded) which provides the ultimate sensitivity for a given power and allows for the  $\sim P_0^{1/2}$  increase in SNR. In other noise regimes the SNR either remains constant with increasing  $P_0$  (intensity-noise regime) or is sub-optimal (detector-noise regime). It is important to note that the shaded area is the desirable parameter space accessible by the hybrid-FRS method, and measurement optimization occurs at the point with the highest SNR.

Within the same parameter space, the FRS signal from  ${}^{\text{P}}\text{P}_1(1)$   $\text{O}_2$  transition is calculated using Eq. (9) and plotted together with the values measured experimentally (Fig. 5(b)).  $2f$  DC-FRS peak signal levels were measured at  $P_{\text{sig}} = 160 \mu\text{W}$ , and the Fig. 5(b) inset shows examples of hybrid-FRS spectra of the  ${}^{\text{P}}\text{P}_1(1)$  line acquired for varying  $\alpha$ . Asymmetries in the line-shape are due to residual intensity modulation of the DFB laser, and peak signal measurements are in excellent agreement with calculations. In Fig. 5(c) an SNR map has been generated using the signal and noise from Fig. 5(b) and 5(a) respectively. It is clear from the figure that conventional balanced-detection that operates at a constant  $\alpha$  (e.g.  $45^\circ$ ) will not approach the highest SNR area through a simple increase of the optical power (the detector saturation level will be reached first). However, for hybrid-FRS which operates at constant  $P_{\text{sig}} = 160 \mu\text{W}$ , the highest SNR that coincides with the line of the available optical power can be conveniently approached. The minimum detection limit (MDL) of  $\text{O}_2$  for each experimental measurement is labeled on the SNR plot and the measured MDL values are in reasonable agreement with the calculated MDL shown in the inset of Fig. 5(c). Taking horizontal cross-sections (fixed  $P_0$ ) of the SNR map, we re-obtain SNR curves shown in Fig. 3(c).

The  $0.6 \text{ ppmv}\cdot\text{Hz}^{-1/2}$  MDL is  $1.4\times$  the shot-noise limit and corresponds to a noise-equivalent polarization rotation  $\Theta_{\text{NEA}} = \sigma_v / [(1 + \gamma) \cdot \sin(2\alpha) \cdot P_0 \cdot G \cdot R_i \cdot H_{2f}] = 1.6 \times 10^{-8} \text{ rad}\cdot\text{Hz}^{-1/2}$  ( $H_{2f} = 0.55$  is signal reduction due to second harmonic detection). We may also calculate the noise-equivalent fractional absorption sensitivity (NEA) for comparison with other methods. For a 6.8 m path length we observe  $\sim 5\%$  optical absorption, which translates to  $\text{NEA} = 1.5 \times 10^{-7} \text{ Hz}^{-1/2}$  and compares very favorably to sensitive absorption spectroscopy techniques [32].

**Table 1. Summary of alternate optical methods to detect atmospheric oxygen.**

Detection Method	Year, [Ref.]	Detection Limit (ppmv)	Averaging Time (sec.)	Comments
BD w/ VCSEL	2001 [12],	35	300	$\sim 60$ x shot-noise limit <sup>1</sup>
QEPAS	2010 [18],	13	> 50	$\sim 1.2$ W laser power 0.21 atm operation
AC-FRS	2010 [26],	10	1	AC coils require $\sim 30$ W
DC-FRS w/ VCSEL	2012 [24],	6	1	1.3 ppmv in 60 sec. 1.13 x shot-noise limit
DC-Hybrid FRS w/ DFB laser diode	2014	0.6	1	1.4 x shot-noise limit < 5 W power consumption

<sup>1</sup>Vogel et. al. [12] claim to be 2.7 to 4 times the shot-noise limit, although their results were obtained by comparing shot-noise in 1 sec. with a 5 min. stability measurement. An estimated actual value is shown in the table above.

## 6. Summary

We have demonstrated and characterized a hybrid-FRS system that combines optimization of the analyzer angle  $\alpha$  with balanced detection. The system detects atmospheric oxygen with an MDL of  $0.6 \text{ ppmv} \cdot \text{Hz}^{-1/2}$  and consumes  $< 5 \text{ W}$  due to application of permanent magnets for magnetic field generation.

We have established hybrid-FRS as a superset of the  $90^\circ$  and  $45^\circ$  FRS detection methods, and the parameter space of operation for our system has been defined. SNR improvements with varying  $\alpha$  and  $P_\theta$  are in good agreement with predictions.

For a given set of experimental parameters, hybrid-FRS will always outperform the  $90^\circ$ -method due to CMRR-suppressed intensity-noise, and eliminates the detector saturation limitation in FRS systems based on  $45^\circ$ -method.

For comparison, Table 1 summarizes alternative atmospheric oxygen detection techniques published in literature. Our result is a  $10\times$  enhancement beyond DC-FRS with a VCSEL emitting only  $200 \mu\text{W}$  [24], and our MDL is also a significant improvement over alternate optical techniques (WMS, QEPAS). Furthermore, FRS is a dispersion-based measurement, thus providing inherently linear response to analyte concentration (in contrast to conventional absorption-based systems, in which the upper bound of dynamic range is limited to  $\leq 10\%$  absorption according to the Beer-Lambert Law) [28, 33]. For higher  $\text{O}_2$  concentrations with absorption of  $> 10\%$  (in our case this corresponds to  $> 40\%$   $\text{O}_2$  levels for 6.8 m path length), power normalization of the FRS signal is required, which can be conveniently implemented using the DC optical signal measured with the photodetectors. Finally, the current hybrid-FRS system requires low power for operation ( $< 5 \text{ W}$ ), making it desirable for field deployable applications.

## Acknowledgments

This work was supported by the NSF-ERC MIRTHE center and from a generous contribution by Lynn and Thomas Ou. The authors are grateful to Prof. Mark Zondlo and Kang Sun for their assistance with the cylindrical mirror multi-pass cell.